Monthly Notices
of the
ROYAL ASTRONOMICAL SOCIETY

MNRAS **493,** 2518–2522 (2020)
Advance Access publication 2020 February 20

doi:10.1093/mnras/staa482

Blueshifted absorption lines from X-ray reflection in IRAS 13224−3809

A. C. Fabian,[1★] C. S. Reynolds,[1] J. Jiang,[1,2] C. Pinto,[3] L. C. Gallo,[4]
M. L. Parker,[5] A. N. Lasenby,[6,7] W. N. Alston,[1] D. J. K. Buisson,[8] E. M. Cackett,[9]
B. De Marco,[10] J. Garcia,[11] E. Kara,[12] P. Kosec,[1] M. J. Middleton,[8] J. M. Miller,[13]
G. Miniutti,[14] D. J. Walton,[1] D. R. Wilkins[15] and A. J. Young[16]

[1] *Institute of Astronomy, Madingley Road, Cambridge CB3 0HA, UK*
[2] *Department of Astronomy, Tsinghua University, 30 Shuangqing Road, Beijing 100034, China*
[3] *INAF – IASF Palermo, Via U. La Malfa 153, I-90146 Palermo, PA, Italy*
[4] *Department of Astronomy and Physics, Saint Mary's University, 923 Robie Street, Halifax, NS B3H 3C3, Canada*
[5] *European Space Agency, European Space Astronomy Centre (ESAC), E-28691 Villanueva de la Cañada, Madrid, Spain*
[6] *Astrophysics Group, Cavendish Laboratory, JJ Thomson Avenue, Cambridge CB3 0HE, UK*
[7] *Kavli Institute for Cosmology, Institute of Astronomy, Madingley Road, Cambridge CB3 0HA, UK*
[8] *Department of Physics and Astronomy, University of Southampton, Highfield, Southampton SO17 1BJ, UK*
[9] *Department of Physics and Astronomy, Wayne State University, 666 W. Hancock Street, Detroit, MI 48201, USA*
[10] *Nicolaus Copernicus Astronomical Center, Polish Academy of Sciences, Bartycka 18, PL-00-716 Warsaw, Poland*
[11] *Cahill Center for Astronomy and Astrophysics, California Institute of Technology, Pasadena, CA 91125, USA*
[12] *MIT Kavli Institute for Astrophysics and Space Research, Cambridge, MA 02139, USA*
[13] *Department of Astronomy, University of Michigan, 1085 S. University, Ann Arbor, MI 48109, USA*
[14] *Centro de Astrobiología (INTA–CSIC), Dep. de Astrofísica, ESAC Campus, E-28692 Villanueva de la Cañada, Spain*
[15] *Kavli Institute of Particle Astrophysics and Cosmology, Stanford University, 452 Lomita Mall, Stanford, CA 94305, USA*
[16] *H.H. Wills Physics Laboratory, Tyndall Avenue, Bristol BS8 1TL, UK*

Accepted 2020 February 14. Received 2020 February 14; in original form 2019 December 20

ABSTRACT

We explore a disc origin for the highly blueshifted, variable absorption lines seen in the X-ray spectrum of the narrow-line Seyfert 1 galaxy IRAS 13224−3809. The blueshift corresponds to a velocity of ∼0.25*c*. Such features in other active galactic nuclei are often interpreted as ultrafast outflows. The velocity is of course present in the orbital motions of the inner disc. The absorption lines in IRAS 13224−3809 are best seen when the flux is low and the reflection component of the disc is strong relative to the power-law continuum. The spectra are consistent with a model in which the reflection component passes through a thin, highly ionized absorbing layer at the surface of the inner disc, the blueshifted side of which dominates the flux due to relativistic aberration (the disc inclination is about 70°). No fast outflow need occurs beyond the disc.

Key words: accretion, accretion discs – black hole physics – galaxies: Seyfert.

1 INTRODUCTION

Outflows are commonly seen around luminous accreting black holes. The gravitational energy released by accretion not only leads to radiation over a wide energy band but also fast winds that, in the case of supermassive black holes, can drive active galactic nucleus (AGN) feedback (for a review see Fabian 2012). The power in an outflow scales as the wind velocity cubed, v^3, so there is considerable interest in ultrafast outflows (UFOs) inferred from blueshifted X-ray absorption features found in a growing number of Seyfert AGN (Pounds et al. 2003, 2016; Reeves et al. 2009; Tombesi et al. 2010, 2013). The velocities derived from the absorption features are typically in the range 0.1–0.3*c*.

UFO-like features have recently been discovered in the *XMM–Newton* European Photon Imaging Camera (EPIC)-pn spectrum of the redshift $z = 0.0658$ narrow-line Seyfert 1 (NLS1) galaxy IRAS 13224−3809 (Parker et al. 2017a). An absorption line at about 8.5 keV, plausibly due to Fe XXVI or Fe XXV, implies a line-of-sight velocity of 0.2–0.25*c*. Blueshifted absorption features due to oxygen and neon are also seen in the *XMM–Newton* Reflection Grating Spectrometer (RGS) spectrum (Pinto et al. 2018) and features due to magnesium, silicon, and sulfur emerged from a principal component analysis (PCA: Parker et al. 2017b) and direct spectral fitting (Jiang et al. 2018) and the rms spectrum of the source (Parker et al. 2020).

A remarkable aspect of the X-ray absorption features is that they are much stronger in the lower half of the large flux range exhibited

---

★ E-mail: acf@ast.cam.ac.uk

Published by Oxford University Press on behalf of the Royal Astronomical Society

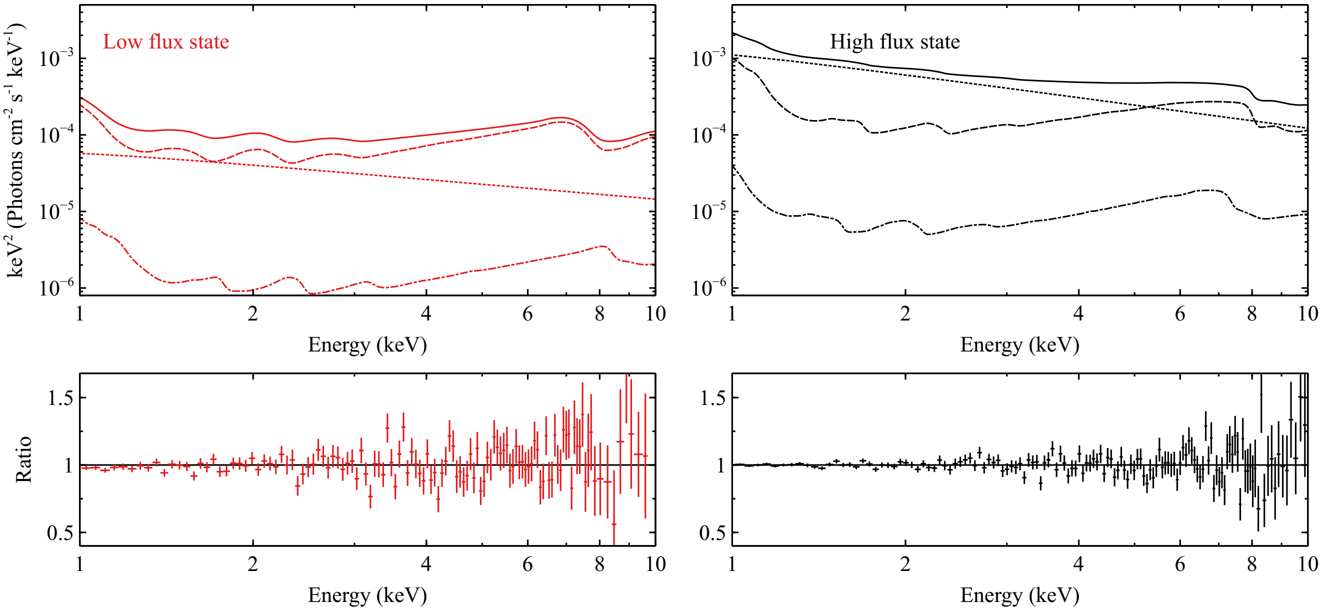

Figure 1. Left-top: the best-fitting model for the low-flux state spectrum (red solid line). Red dashed line: the absorbed reflection emission from the inner region of the disc; red dash–dotted line: the unabsorbed reflection emission from the outer region of the disc; red dotted line: power-law continuum emission. Left-bottom: the data/model ratio plot for the low-flux state spectrum. Right: same as the left-hand panels but for the high-flux state spectrum.

Table 1. Best-fitting parameters for the low-flux state and the high-flux state spectra. A single emissivity index is used for RELCONV, i.e. $q = q_1 = q_2$.

Model	Parameter	Unit	Low flux	High flux
RELCONV	q	–	>4	4 ± 2
	$R_{\rm out}$	$r_{\rm g}$	<7	3 (fixed)
	i	$\circ$	71 ± 3	70 ± 2
XSTAR1	$N_{\rm H,\,1}$	10^{23} cm^{-2}	8 ± 2	4 ± 2
	$\log(\xi_1')$	log(erg cm s^{-1})	3.9 ± 0.3	3.9 ± 0.4
XSTAR2	$N_{\rm H,\,2}$	10^{23} cm^{-2}	4^{+2}_{-1}	<2
	$\log(\xi_2')$	log(erg cm s^{-1})	$3.4^{+0.2}_{-0.1}$	3.4 (fixed)
XILLVERD1	$\log(\xi)$	log(erg cm s^{-1})	1.0 ± 0.3	$1.0^{+0.1}_{-0.6}$
	$Z_{\rm Fe}$	$Z_\odot$	3 ± 1	4^{+1}_{-2}
	norm	–	$5.6^{+0.4}_{-0.8} \times 10^{-5}$	$1.23^{+0.10}_{-0.08} \times 10^{-3}$
XILLVERD2	norm	–	$<3 \times 10^{-6}$	$<1.5 \times 10^{-4}$
POWERLAW	Γ	–	$2.74^{+0.03}_{-0.04}$	$3.00^{+0.07}_{-0.06}$
	norm	–	$(6 \pm 1) \times 10^{-5}$	$1.24^{+0.08}_{-0.04} \times 10^{-3}$
	χ^2/ν		112.84/110	131.98/120

by the highly variable source (Parker et al. 2017a; Jiang et al. 2018; Pinto et al. 2018). This could be due to the gas becoming increasingly photoionized as the source luminosity increases or to geometry if the brightening is associated with the X-ray emitting corona increasing in height above the disc (Pinto et al. 2018).

A radical alternative interpretation is that the absorbing gas is not outflowing at all but merely circulating at the surface of the accretion disc (Gallo & Fabian 2011, hereafter GF11; Gallo & Fabian 2013). The orbital velocity of the disc increases up to 0.5c at the innermost stable circular orbit (ISCO) and so all velocities below that are present in the disc. Observable UFO velocities of 0.2–0.3c are reached within radii of 10$r_{\rm g}$ around a black hole, where $r_{\rm g} = GM/c^2$. Doppler beaming makes the approaching side of the disc brightest, hence absorbing corotating gas along our line of sight to those radii of the disc can produce a blueshifted absorption line (GF11).

In this paper, we apply this model to spectra of the lowest and highest flux states of IRAS 13224−3809.

2 SIMPLE X-RAY SPECTRAL MODELLING OF DISC ABSORPTION IN IRAS 13224−3809

We modelled the 2016 *XMM–Newton* flux-resolved EPIC-pn spectra of IRAS 13224−3809 between 1 and 10 keV in order to focus on the broad iron absorption feature seen at 8 keV (Parker et al. 2017a) and a series of blueshifted absorption features at 1–4 keV (i.e. Si XIV, S XVI lines; Jiang et al. 2018; Pinto et al. 2018). The data have been gathered into three spectra representing low, medium, and high flux, each with a similar number of counts (Parker et al. 2017a).

First, we use the disc emission model from Jiang et al. (2018). This involves the high-density disc reflection model XILLVERD (Garcia et al. 2016) with the electron density fixed at $n_{\rm e} = 10^{19}$ cm^{-3} during the fit (Jiang et al. 2018). The disc emission consists of two components: one from the inner region with an absorption layer on top (XILLVERD1), and the other one from the outer region that is not affected by absorption (XILLVERD2). We assume the same density and ionization state for the two regions of the disc.

Second, two photoionized-plasma absorption models XSTAR are constructed and fitted in XSPEC. These absorption models are only applied to XILLVERD1. The XSTAR models assume solar abundances except for that of iron and an ionizing luminosity of 10^{43} erg s^{-1}. A power law with $\Gamma = 2$ is assumed for the ionizing spectrum. The redshift parameter (z) of the absorption models is fixed at the source redshift ($z = 0.066$). Free parameters are the ionization of the plasma (ξ'[1]), the column density ($N_{\rm H}$), and the iron abundance ($Z_{\rm Fe}'$, which is linked to that of the disc). Note that the solar abundances of XSTAR and XILLVERD are both taken from Grevesse & Sauval (1998).

---

[1] The prime symbol is to distinguish the parameters of the absorbers from those of the disc reflection models.

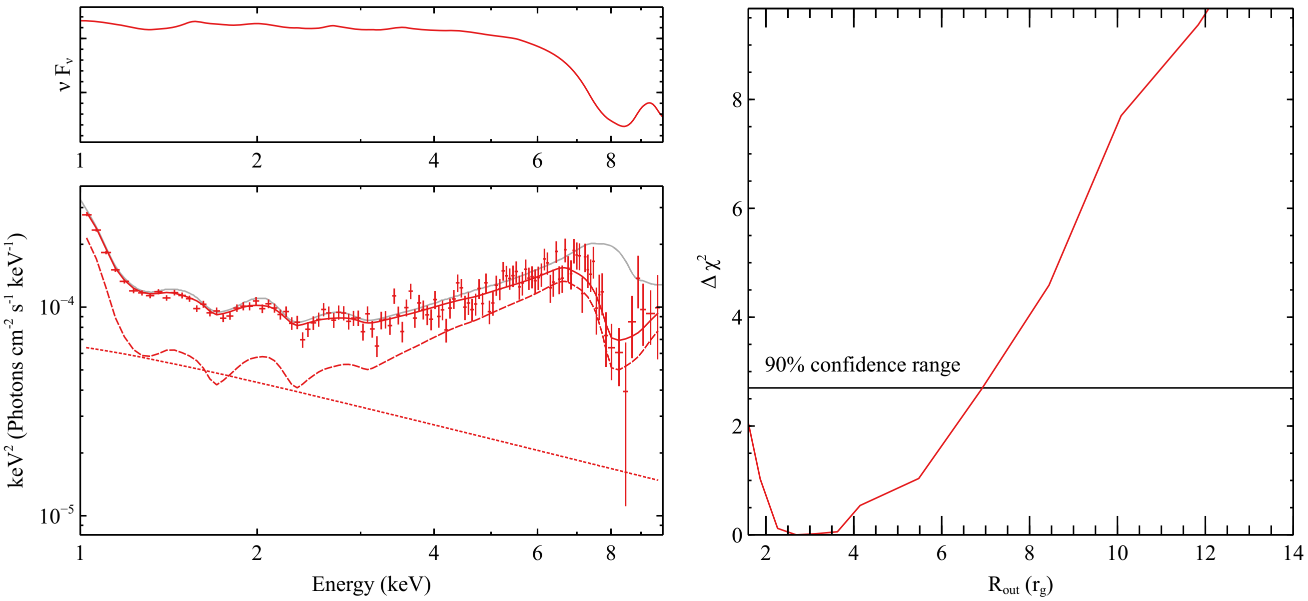

Figure 2. Top-left: the best-fitting absorption model for the low-flux state spectrum applied to a power law with $\Gamma = 2$ to show the shape of the absorption lines. The normalization of the model is arbitrary in this figure. Bottom-left: the best-fitting model for the low-flux state spectrum (red solid line). Only the reflection from the inner disc (dashed line) and the power-law emission (dotted line) are shown for clarity. The unfolded low-flux state spectrum is shown as red crosses for comparison with the model. Right: χ^2 as a function of the maximum disc radius of the absorption zone. The inner radius of the annular absorber is fixed at the innermost stable circular orbit (ISCO; $1.5r_g$).

Third, the RELCONV model (Dauser 2013) is used to apply relativistic effects to the rest-frame reflection spectra. The total model is TBABS∗(RELCONV∗XSTAR1∗XSTAR2∗XILLVERD1+RELCONV∗XILLVERD2+POWRLAW) in the XSPEC format. The inner radius parameter of the first RELCONV is set at the radius of the ISCO ($R = 1.5r_g$ for $a = 0.98$), while the outer radius is a free parameter. The inner radius of the second RELCONV equals the outer radius parameter of the first, and its outer radius is fixed at $400r_g$. All the other parameters in the RELCONV models are linked.

The best-fitting models and the corresponding ratio plots can be found in Fig. 1, and the best-fitting parameters are shown in Table 1. The models describe both the low-flux state and the high-flux state spectra very well.

For the low-flux state spectrum, the best-fitting power-law continuum has a photon index of 2.74. The ionization of the disc reflection component is low with $\xi = 10$ erg cm s^{-1} and an iron abundance of ≈3 compared to solar. A similar high disc inclination (71°) is obtained as for previous work (i.e. $i = 67° \pm 3°$ obtained by fitting with REFLIONX; Jiang et al. 2018). As shown in the top left-hand panel of Fig. 2, the flux of the reflection from the inner region (XILLVERD1) is more than 10 times higher than the reflection from the outer region (XILLVERD2). The former is exposed to an ionized absorption layer of $N_{\mathrm{H},\,1;\,2} = 4$–$8 \times 10^{23}$ cm^{-2} and $\log \xi = 3.4$–3.9 in the rest frame of the disc. The column density of these two absorbers is much higher than the values obtained by the outflow model (e.g. $N_{\mathrm{H}} \approx 10^{22}$ cm^{-2}; Jiang et al. 2018).

In order to better demonstrate how disc absorption works, we apply our best-fitting absorption models (KDBLUR1∗XSTAR1∗XSTAR2) to a power law with $\Gamma = 2$ and show the model in the top panel[2] of Fig. 2. The best-fitting absorption model predicts very broad Fe XXV/XXVI absorption lines, which correspond to the line features between 8 and 9 keV in the real data. The red wing of the broad Fe XXV/XXVI absorption line extends to 6 keV, and affects the blue wing of the broad Fe K emission line in the reflection component. In the bottom left-hand panel, we show the best-fitting model in comparison with the unfolded low-flux state spectrum. The right-hand panel of Fig. 2 shows χ^2 as a function of the maximum disc radius of the absorption zone. The best-fitting outer radius of the absorbers is around $3r_g$ with a 90 per cent confidence range of $<7r_g$, which suggests the absorbing zone is in the innermost region of the disc within a few r_g.

For the high-flux state spectrum, the best-fitting power-law continuum has a softer photon index ($\Gamma = 3$) compared with the low-flux state spectrum. The ionization of the disc reflection component remains consistently low. The relativistic iron line shows an emissivity profile that is consistent with a power law of $q = 4$. A lower column density is required for the first absorber, and a larger uncertainty of the ionization is found. By fixing the ionization of the second absorber at the best-fitting value for the low-flux state spectrum, we obtain an upper limit of the column density, suggesting weaker absorption in the high-flux state. This result is consistent with previous work (Parker et al. 2017a; Jiang et al. 2018; Pinto et al. 2018). The outer radius of the absorption zone is not constrained due to the low reflection fraction in the high-flux state (compare the models for two flux states in Fig. 1), and thus R_{out} is fixed at the best-fitting value for the low-flux state spectrum.

3 A PHYSICALLY MOTIVATED MODEL

The above modelling shows that highly ionized absorption applied only to the reflection component is consistent with the low-flux spectrum. Such absorption becomes undetectable in the high state due to a combination of (a) reduction in the column density of the absorber and (b) dilution by the power-law continuum, which

---

[2] A power law with $\Gamma = 2$ would be a horizontal line in the figure. This choice of photon index is only for illustration. We adopt an arbitrary normalization for the power-law model.

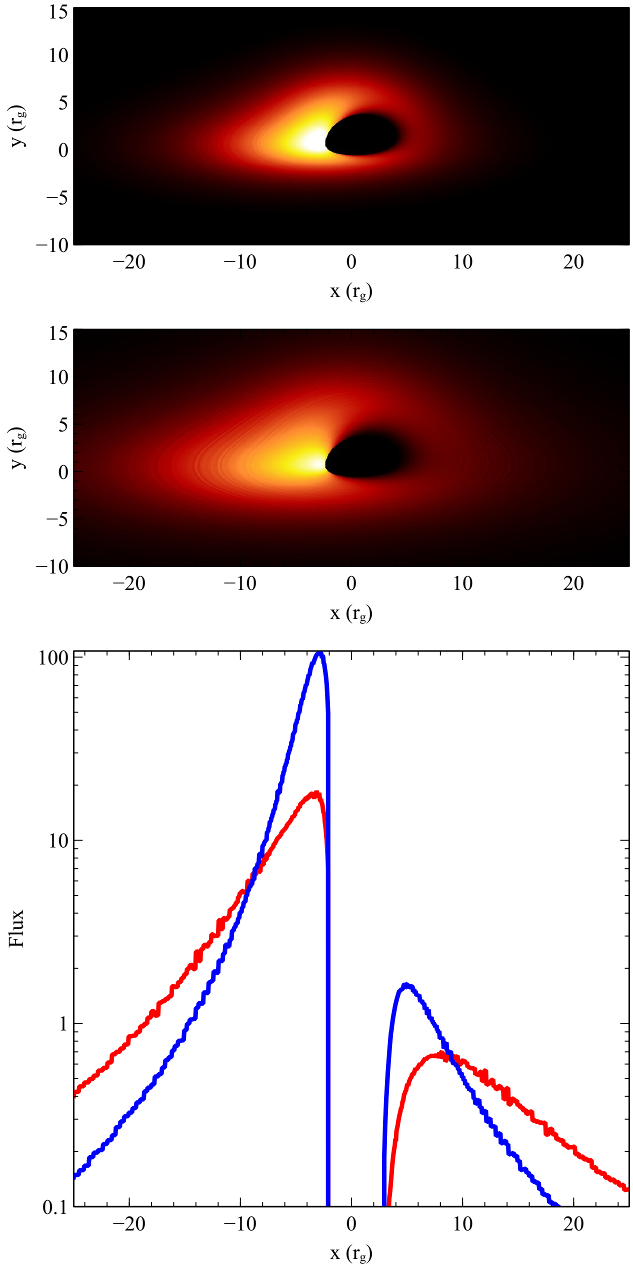

Figure 3. Top: intensity-weighted image of a disc irradiated by a corona at height $h = 4r_g$, appropriate for the low-flux state. The colour table is logarithmic spanning a range of 1000 from white to dark red. *x* and *y* are in the image plane. Centre: similar plot for $h = 10r_g$ to represent the high-flux state. Bottom: flux profiles along a mid-plane cut. Blue line is $h = 4r_g$ lamp post; red line is $h = 10r_g$.

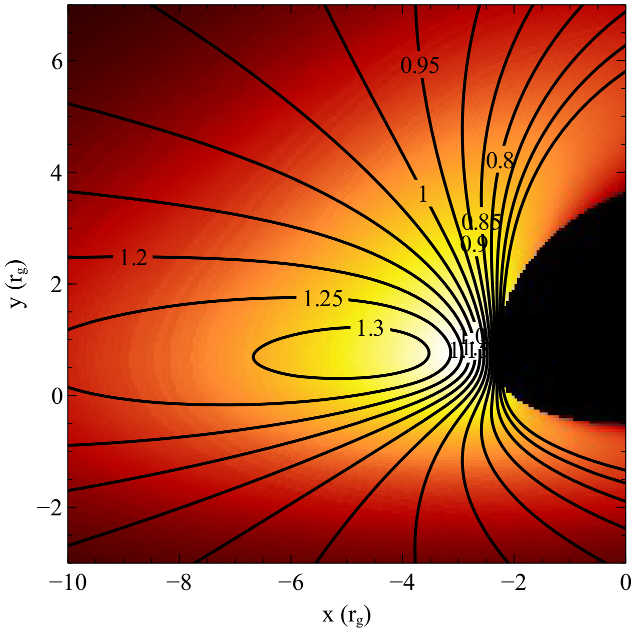

Figure 4. The approaching side of the disc shown in the top panel of Fig. 3 overlaid with contours showing the *g*-factor at the surface of the disc in the rest frame of the source. $g = E_{\rm obs}/E_{\rm em}$ and is about 1.27 at the line centre. *E* is photon energy, *x* and *y* are in the image plane.

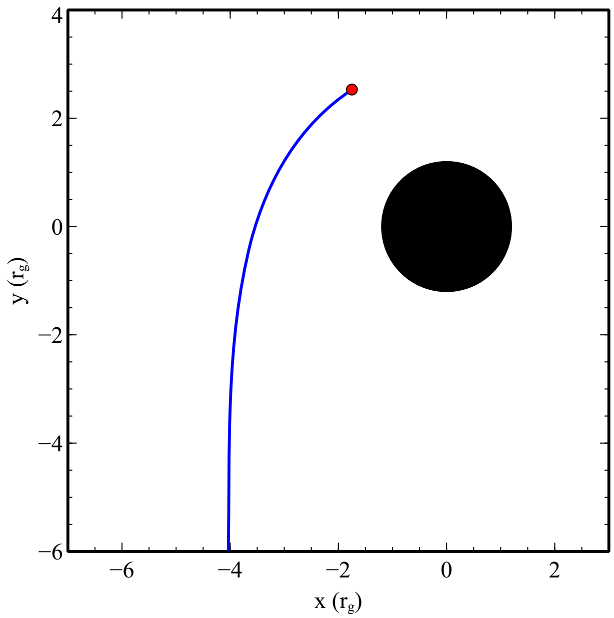

Figure 5. Path of a photon from the brightest part of the reflection emission region (Fig. 3, top). The observer lies off the bottom. *x* and *y* here are in the frame of the disc.

becomes relatively stronger. The 1–10 keV power-law continuum increases by a factor of 13 from low to high state, whereas the reflection component increases by a factor of only 3. At 8.5 keV where the Fe K absorption feature appears, the factors are 6.9 and 2.1, respectively (see Fig. 1).

We assume that the absorbing gas shares the orbital velocity of the disc immediately below it. Fig. 2 (right) shows that the detectable absorber extends in radius from about 2 to $7r_g$. (There may be undetected absorption at larger radii from lower column density material.) An image (computed using the code from Reynolds et al. 1999) showing how the region appears to the observer is shown in Fig. 3: the disc is irradiated by a corona (not shown) located along the spin-axis at a height of $\sim 5r_g$ above its centre (Alston et al. 2020). The brightest part of the reflection corresponds to the region with the highest blueshift that also lies between about 2 and $8r_g$ from the black hole along the *apparent* approaching mid-line of the disc (Figs 3 and 4). It is *apparent* because the path of a photon appearing to the observer to originate from the brightest part of the disc originates behind the black hole, due to light bending in the Kerr metric (see Fig. 5).

The high-flux state corresponds to the coronal height being about $10r_g$. Its radius will also be larger. The reflection component then no longer originates from a small part of the inner disc but is more spread out (Fig. 3, middle and lower plots), contributing further to the lack of an observed absorption feature in the high state.

A high inclination is required for UFO-like features to be seen. At the inclination of $\sim 71^\circ$ inferred for IRAS 13224−3809, the total *vertical* column density of absorbing matter in the low state is $\sim 4 \times 10^{23}$ cm^{-2}, which corresponds to a Thomson depth[3] of about 0.3. It may be less in the high state. (Any contribution by the absorber to the total reflection component can therefore be neglected.) The absorber has an ionization parameter about 1000 times higher than the disc, so the absorption density must be about 10^{16} cm^{-3}. The depth of the absorbing region is then only $\sim 3 \times 10^7$ cm, or $\sim 10^{-4} r_g$, if the black hole mass is 2×10^6 M$_\odot$ (Alston et al. 2020). Our fits require two absorbers representing a factor of 3 range of ionization parameter that means a corresponding range of density in the absorbing layer. We assume that the absorbing layer lies immediately above the surface of the dense disc.

Absorption is imprinted on the reflection spectrum both as radiation enters the disc and as it leaves it. Assuming that much of the incoming radiation is incident vertically on the disc and that the observed radiation is from an angle near 70°, then 3/4 of the total absorbing column density traversed is found as it leaves the disc. This means that the above depth is overestimated by about 30 per cent.

4 DISCUSSION

We conclude that a plausible origin for the variable blueshifted absorption in IRAS 13224−3809 lies in a thin, low density, outer layer of the inner accretion disc. Our line of sight to the brightest part of the reflection component passes through regions above the disc where absorbing matter corotating with the disc would appear blueshifted by the observed value.

The model may apply to other detected UFOs, particularly if strong, compact, inner reflection components are present and the disc inclination and spin are high. UFOs reported from objects that have no reflection component are likely to be genuine outflows, such as the case for the highly blueshifted absorption seen in ultraluminous X-ray (ULX) sources (Pinto, Middleton & Fabian 2016; Walton et al. 2016; Kosec et al. 2018). Moreover, any low-density absorbing gas must not be so highly ionized that few ions are available to cause absorption features. This may occur in luminous stellar mass black hole systems where the disc tends already to have a high ionization parameter and any lower density gas above it would be even more highly ionized.

The situation for observing ultrafast disc absorption features is optimized when the brightest part of the reflection component is highly localized on the approaching side of the disc and the inclination is high enough for our line of sight to intercept a sufficient column density of absorber above the disc. This implies a compact corona at a small height above the black hole.

Although IRAS 13224−3809 may be above the Eddington limit, much of the radiation in the inner region originates in the corona, which lies above the disc and radiates down on it. This geometry minimizes radiation-driven outflows from the disc.

The rms spectrum of IRAS 13224−3809 (Parker et al. 2020) shows that the absorption line is strongly variable, 30 per cent more than the neighbouring continuum. This may reflect rapid variations in the disc surface.

Disc absorption presents a new feature of X-ray reflection. The highly blueshifted features found in IRAS 13224−3809 represent a probe of the innermost accretion flow *within a few gravitational radii of the black hole*. High-resolution spectra obtained by future missions, such as the *X-Ray Imaging and Spectroscopy Mission* (*XRISM*) and *Athena*, will potentially resolve the line shape of the broad absorption line features, locating and mapping the disc absorber with high accuracy.

ACKNOWLEDGEMENTS

We thank the referee for helpful comments. WNA and ACF acknowledge support from ERC Advanced Grant FEEDBACK, 340442. JJ acknowledges support from the Tsinghua Astrophysics Outstanding Fellowship and the Tsinghua Shuimu Scholar Programme. JJ also acknowledges support from the Cambridge Trust and the Chinese Scholarship Council Joint Scholarship Programme (201604100032). CSR thanks the UK Science and Technology Facilities Council (STFC) for support under the New Applicant grant ST/R000867/1, and the European Research Council (ERC) for support under the European Union's Horizon 2020 research and innovation programme (grant 834203). PK acknowledges support from the STFC. BDM acknowledges support from the European Union's Horizon 2020 Research and Innovation Programme under the Marie Sklodowska-Curie grant agreement no. 798726. GM acknowledges funding by the Spanish State Research Agency (AEI) Project No. ESP2017-86582-C4-1-R and No. MDM-2017-0737 Unidad de Excelencia 'María de Maeztu' – Centro de Astrobiología (CSIC-INTA).

REFERENCES

Alston W. N. et al., 2020, Nat. Astron., in press (arXiv:2001.06454)
Dauser T. et al., 2013, MNRAS, 430, 1693
Fabian A. C., 2012, ARA&A, 50, 455
Gallo L. C., Fabian A. C., 2011, MNRAS, 418, L59 (GF11)
Gallo L. C., Fabian A. C., 2013, MNRAS, 434, L66
Garcia J., Fabian A. C., Kallman T. R., Dauser T., Parker M. L., McClintock J. E., Steiner J. F., Wilms J., 2016, MNRAS, 462, 751
Grevesse N., Sauval A. J., 1998, Space Sci. Rev., 85, 161
Jiang J. et al., 2018, MNRAS, 477, 3711
Kosec P. et al., 2018, MNRAS, 479, 3978
Parker M. L. et al., 2017a, Nature, 543, 83
Parker M. L. et al., 2017b, MNRAS, 469, 1553
Parker M. L., Alston W. N., Igo Z., Fabian A. C., 2020, MNRAS, 492, 1363
Pinto C., Middleton M. J., Fabian A. C., 2016, Nature, 533, 64
Pinto C. et al., 2018, MNRAS, 476, 1021
Pounds K. A., Reeves J. N., King A. R., Page K. L., O'Brien P. T., Turner M. J. L., 2003, MNRAS, 345, 705
Pounds K. A., Lobban A., Reeves J., Vaughan S., 2016, MNRAS, 457, 2951
Reeves J. N. et al., 2009, ApJ, 701, 493
Reynolds C. S., Young A. J., Begelman M. C., Fabian A. C., 1999, ApJ, 514, 164
Tombesi F., Cappi M., Reeves J. N., Palumbo G. G. C., Yaqoob T., Braito V., Dadina M., 2010, A&A, 521, A57
Tombesi F., Cappi M., Reeves J. N., Nemmen R. S., Braito V., Gaspari M., Reynolds C. S., 2013, MNRAS, 430, 1102
Walton D. J. et al., 2016, ApJ, 826, L26

This paper has been typeset from a TEX/LATEX file prepared by the author.

---

[3] XSTAR does not currently include the effects of electron scattering, which will slightly affect the inferred column densities.